

Robust Grasping by Bimanual Robots with Stable Parametrization-Based Contact Servoing

Anqing Duan, Shengzeng Huo, Hoiyin Lee, Peng Zhou, *Member, IEEE*, Jose Guadalupe Romero, Chenguang Yang, *Senior Member, IEEE*, and David Navarro-Alarcon, *Senior Member, IEEE*

Abstract—Robots with bimanual morphology usually possess higher flexibility, dexterity, and efficiency than those only equipped with a single arm. The dual-arm structure has enabled robots to perform various intricate tasks that are difficult or even impossible to achieve by uni-manipulation. In this paper, we address the robust bimanual grasping problem for the task of object transportation. Specifically, since stable contact is the key to the success of the transportation task, our focus lies on stabilizing the contact established between the object and the robot end-effectors. To ensure that the contact is stable, the contact wrenches are required to evolve within the so-called friction cones all the time throughout the transportation task. To this end, we propose stabilizing the contact by leveraging a novel contact parametrization model. The parametrization expresses the contact stability manifold with a set of constraint-free exogenous parameters where the mapping is bijective. Notably, such parametrization can guarantee that the contact stability constraints can always be satisfied. We also show that many commonly used contact models can be parametrized out of a similar principle. Furthermore, to exploit the parametrized contact models in the control law, we devise a contact servoing strategy for the bimanual robotic system such that the force feedback signals from the Force/Torque sensors are incorporated into the control loop. The effectiveness of the proposed approach is well demonstrated with the experiments on several representative bimanual transportation tasks.

Index Terms—Bimanual Manipulation; Contact Modelling; Force Control; Direct/Inverse Dynamics Formulation.

I. INTRODUCTION

Bimanual manipulation has been an active research area in the field of robotics and mechatronics. With the help of an additionally equipped arm, a dual-arm robotic system possesses many merits compared with a single robot arm, such as flexible distribution of payload, adjustable contact support, and efficient task execution, among others [1]. It has been observed that bimanual robots can accomplish a wide range of complicated tasks, such as deformable objects shaping [2]–[4], stir-fry cooking [5], electric cable routing [6], floor sweeping [7], clothes folding [8], components screwing [9], wrench balancing [10], just to name a few.

This work is supported in part by the Research Grants Council (RGC) of Hong Kong under grants 15212721 and 15231023, and in part by the Jiangsu Industrial Technology Research Institute Collaborative Scheme under grant K-ZG9V. *Corresponding author: D. Navarro-Alarcon.*

A. Duan, S. Huo, H. Lee, P. Zhou, and D. Navarro-Alarcon are with the Department of Mechanical Engineering, The Hong Kong Polytechnic University, KLN, Hong Kong (e-mail: dna@ieec.org).

J. G. Romero is with the Digital Systems Department, Instituto Tecnológico Autónomo de México (ITAM), Mexico City, Mexico.

C. Yang is with Bristol Robotics Laboratory, University of the West of England, Bristol, BS16 1QY, UK (e-mail: cyang@ieec.org).

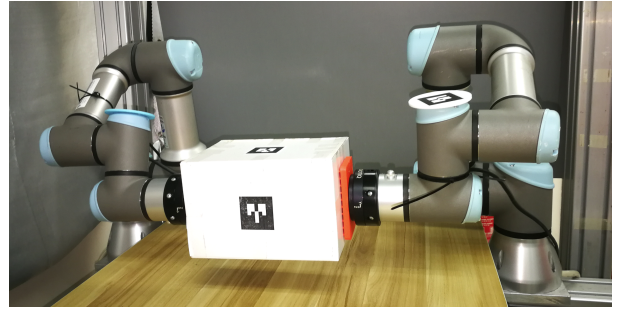


Fig. 1. Illustration of robotic bimanual manipulation.

Following the taxonomy developed by [11], bimanual manipulation can be technically classified into the following categories in terms of the so-called *action vocabulary*: i) Fixed offset where the relative configuration between two hands remains constant or does not exhibit much change; ii) One hand fixed where one hand is relatively stationary and mostly used for providing contact support whilst the other hand exhibits a more active motion pattern; iii) Self-handover where an object is passed from one hand to the other with two hands coming together first and then separating apart later; iv) One hand seeking where one hand reaches towards an object with the other one being either supernumerary or a counterweight. In this paper, we particularly focus on bimanual manipulation under the category of fixed offset, as shown in Fig. 1. More precisely, we address the object transportation task, which dictates the offset between two hands to be constrained due to the rigid object being held [12].

By imposing a fixed-offset constraint on the movement of two end-effectors, explicit coordination between two arms will be required. Following this direction, various algorithms have been developed for the coordination of two or even more robot arms, such as dynamical systems [13], task-parameterized Gaussian mixture model [14], and graph attention network [15]. Although the works above have achieved promising results on the coordination of two arms, they mainly deal with dual-arm manipulation through trajectory-level imitation [16], which overlooks the issue of maintaining contact between robot arms and the object.

Contact modeling usually plays a critical role in robust manipulation [17], as a broken contact would potentially make the object drop from the end-effectors. Many notions have been proposed to guarantee contact stability, such as internal force regulation [18], grasp wrench decomposition [19], static robust polyhedron [20], rectangular sup-

porting areas [21], and friction cone stability margin [22]. Compared with these approaches, our method stabilizes the contact wrench by explicitly modeling its dynamics based on a parametrization model. The central idea of the parametrization technique is to transcribe the contact-induced constraints with a set of constraint-free exogenous parameters by leveraging the boundedness property of some function. A similar strategy has also been successfully applied to other robotic applications, including biped locomotion [23] and constrained imitation learning [24]. In this paper, we demonstrate that such a contact parametrization approach can be employed to facilitate fixed-offset bimanual manipulation. Specifically, we demonstrate the proposed method for the case of unilateral planar contact as it is encompassing. It can be readily shown that other commonly encountered rigid contact models can be parametrized based on a similar principle.

From the perspective of control design, various control strategies have been developed for bimanual manipulation, such as coordinated compliance control [25], projected force-admittance control [26], adaptive neural control [27], deep imitation control [28], etc. It is noted, however, that stabilization of the interaction forces is usually not explicitly taken into account by these control strategies. We propose to design a control law that exploits the proposed contact parametrization model with the rate of change of the exogenous variables being the virtual control signals. The convergence of the devised control law can be shown in the sense of Lyapunov.

In summary, the original contributions of this paper are outlined as follows:

- We propose a class of novel contact parametrization models complying with contact stability manifolds, that simplify the representation of contact friction cones;
- We present a new bimanual control strategy featured by contact servoing that incorporates force feedback and exploits the proposed contact parametrization model;
- We report an experimental study to validate our proposed methodology with fixed-offset bimanual manipulation.

The rest of the paper is organized as follows: Section II presents the overall system modeling for bimanual manipulation control. The stability-guaranteed contact parametrization approach is then introduced in Section III. Subsequently, the control strategy with contact-servoing to exploit force feedback is developed in Section IV. The experimental studies on the effectiveness of the proposed approach are reported in Section V. Finally, Section VI concludes the paper. The key notation used throughout the paper is summarized in Table I.

II. SYSTEM MODELING

We assume that the dual-arm robotic system is composed of a left arm and a right arm (see Fig. 2). Both arms are fixed base with respect to the world inertial frame \mathcal{W} . The joint configurations are characterized by $q_l \in \mathbb{R}^{nl}$ and $q_r \in \mathbb{R}^{nr}$ with the degree of freedom being nl and nr , respectively. When an object is held between the left and right end-effectors, the configuration of the whole system, consisting of both the arms and the object, is expressed as $(q_l, {}^{\mathcal{W}}O_{\mathcal{O}}, {}^{\mathcal{W}}R_{\mathcal{O}}, q_r) \in \mathbb{R}^{nl} \times \mathbb{R}^3 \times SO(3) \times \mathbb{R}^{nr}$, where $({}^{\mathcal{W}}O_{\mathcal{O}}, {}^{\mathcal{W}}R_{\mathcal{O}}) \in SE(3)$

TABLE I
KEY NOTATION

Symbol	Definition
$\mathcal{W}, \mathcal{O}, \mathcal{C}, E$	Frames of the world, object, contact, and end-effector
$\mathbb{1}_n, \mathbf{0}_{m \times n}$	The identity matrix and the zero matrix
Ad_g^T	The adjoint matrix transforming wrenches from B to A
$S(\cdot), (\cdot)^\vee$	The skew-symmetric operation and its inverse operator
${}^A R_B$	The rotation matrix expressing vectors from B to A
$A[B]$	The frame with the origin as A and the rotation as B
e_i	The canonical base with the i -th element being unitary
$\mathcal{N}(\cdot)$	The null-space projection operator

expressed in \mathcal{W} represent the coordinates of the origin and orientation of the object frame \mathcal{O} rigidly attached at the center of mass of the object.

We compactly express dual-arm dynamics by concatenating individual manipulator dynamics. More precisely, the dynamics model of two arms interacting with the held object can then be modeled as [29]

$$M_a(q)\ddot{q} + C_a(q, \dot{q})\dot{q} + g_a(q) = \tau + J_a^T f_c, \quad (1)$$

where we have

$$M_a = \begin{bmatrix} M_l(q_l) & 0_{nl \times nr} \\ 0_{nr \times nl} & M_r(q_r) \end{bmatrix} \quad C_a = \begin{bmatrix} C_l(q_l, \dot{q}_l) & 0_{nl \times nr} \\ 0_{nr \times nl} & C_r(q_r, \dot{q}_r) \end{bmatrix} \quad (2)$$

$$q = \begin{bmatrix} q_l \\ q_r \end{bmatrix} \quad g_a = \begin{bmatrix} g_l(q_l) \\ g_r(q_r) \end{bmatrix} \quad \tau = \begin{bmatrix} \tau_l \\ \tau_r \end{bmatrix} \quad f_c = \begin{bmatrix} f_{cl} \\ f_{cr} \end{bmatrix}$$

where $M_l \in \mathbb{R}^{nl \times nl}$ and $M_r \in \mathbb{R}^{nr \times nr}$ are the mass matrices, $C_l \in \mathbb{R}^{nl \times nl}$ and $C_r \in \mathbb{R}^{nr \times nr}$ are the Coriolis matrices, $g_l \in \mathbb{R}^{nl}$ and $g_r \in \mathbb{R}^{nr}$ are the gravity terms, $\tau_l \in \mathbb{R}^{nl}$ and $\tau_r \in \mathbb{R}^{nr}$ are the joint actuator torques for the left and right arm, respectively. In order to ensure that the contacts between the object and the end-effectors are firm, the contact forces f_{cl} and f_{cr} must be restricted within the so-called friction cones $\mathcal{FC}_{cl} \subset \mathbb{R}^{ncl}$ and $\mathcal{FC}_{cr} \subset \mathbb{R}^{ncr}$, where ncl and ncr indicate the number of independent forces that can be applied by the left and right contact, respectively. The friction cone constraint can be compactly written as

$$f_c \in \mathcal{FC}_{lr} \quad \text{with} \quad \mathcal{FC}_{lr} = \mathcal{FC}_{cl} \times \mathcal{FC}_{cr}. \quad (3)$$

Notice that satisfaction of the constraints due to friction cone plays an important role in the success of bimanual task execution, which remains a central topic of this paper.

Furthermore, the *arm Jacobian*, whose transpose relates the contact forces to the joint-space torques, is given by

$$J_a = \begin{bmatrix} B_{cl}^T Ad_{g_{elcl}}^{-1} Ad_{g_{w_{tel}}}^{-1} J_l & 0_{ncl \times nr} \\ 0_{ncr \times nl} & B_{cr}^T Ad_{g_{ercr}}^{-1} Ad_{g_{w_{rer}}}^{-1} J_r \end{bmatrix} \quad (4)$$

where $J_l \in \mathbb{R}^{6 \times nl}$ and $J_r \in \mathbb{R}^{6 \times nr}$ denote the Jacobian matrices that map the individual arm's joint velocities \dot{q}_l and \dot{q}_r to the linear and angular velocities of the end-effector frames E_l and E_r . Besides, $B_{cl} \in \mathbb{R}^{6 \times ncl}$ and $B_{cr} \in \mathbb{R}^{6 \times ncr}$ represent the wrench basis. In addition, $Ad_g \in \mathbb{R}^{6 \times 6}$ denotes the adjoint transformation matrix as a change of frame. Particularly, $Ad_{g_{elcl}}^T$ and $Ad_{g_{ercr}}^T$ transform the wrenches expressed in the contact frames \mathcal{C}_l and \mathcal{C}_r into ones expressed in end-effector frames E_l and E_r ; $Ad_{g_{w_{tel}}}^T$ and $Ad_{g_{w_{rer}}}^T$ transform

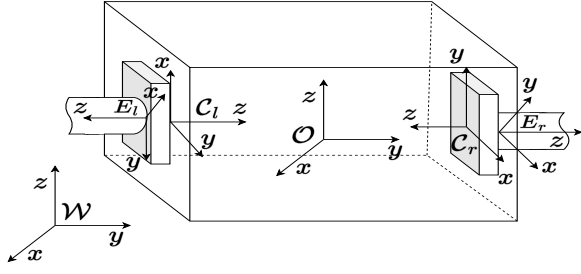


Fig. 2. Illustration of world, object, contact, and end-effectors frames.

the wrenches expressed in the end-effector frames E_l and E_r into ones expressed in the frames $E_l[\mathcal{W}]$ and $E_r[\mathcal{W}]$.

For object dynamics modeling, we resort to the law of motion that the rate of change of momentum is equal to the summation of all the external wrenches applied. Recall first that the momentum ${}^{\mathcal{O}[\mathcal{W}]}h$ expressed with respect to $\mathcal{O}[\mathcal{W}]$ is composed of a linear momentum ${}^{\mathcal{O}[\mathcal{W}]}P$ and an angular momentum ${}^{\mathcal{O}[\mathcal{W}]}L$

$${}^{\mathcal{O}[\mathcal{W}]}h = \begin{bmatrix} {}^{\mathcal{O}[\mathcal{W}]}P \\ {}^{\mathcal{O}[\mathcal{W}]}L \end{bmatrix} = \begin{bmatrix} m_{\mathcal{O}} {}^{\mathcal{W}}\dot{o}_{\mathcal{O}} \\ {}^{\mathcal{O}[\mathcal{W}]}I {}^{\mathcal{W}}\omega_{\mathcal{O}} \end{bmatrix} \in \mathbb{R}^6, \quad (5)$$

where $m_{\mathcal{O}}$ denotes the mass of the object that is known *a priori*, ${}^{\mathcal{W}}\omega_{\mathcal{O}}$ is the angular velocity of the frame \mathcal{O} with respect to \mathcal{W} , and more precisely, we have ${}^{\mathcal{W}}\dot{R}_{\mathcal{O}} = S({}^{\mathcal{W}}\omega_{\mathcal{O}}) {}^{\mathcal{W}}R_{\mathcal{O}}$. ${}^{\mathcal{O}[\mathcal{W}]}I = {}^{\mathcal{W}}R_{\mathcal{O}} I_{\mathcal{O}} {}^{\mathcal{W}}R_{\mathcal{O}}^T$ is instantaneous inertia tensor relative to $\mathcal{O}[\mathcal{W}]$ where $I_{\mathcal{O}}$ is the inertia tensor of the object expressed in the body frame \mathcal{O} .

By differentiating (5) with respect to time, the momentum rate of change can be obtained as

$$\begin{aligned} {}^{\mathcal{O}[\mathcal{W}]} \dot{h} &= \begin{bmatrix} {}^{\mathcal{O}[\mathcal{W}]} \dot{P} \\ {}^{\mathcal{O}[\mathcal{W}]} \dot{L} \end{bmatrix} = \begin{bmatrix} m_{\mathcal{O}} {}^{\mathcal{W}} \ddot{o}_{\mathcal{O}} \\ {}^{\mathcal{O}[\mathcal{W}]} I {}^{\mathcal{W}} \dot{\omega}_{\mathcal{O}} + S({}^{\mathcal{W}} \omega_{\mathcal{O}}) {}^{\mathcal{O}[\mathcal{W}]} I {}^{\mathcal{W}} \omega_{\mathcal{O}} \end{bmatrix} \\ &= Gf_c - mge_3 \end{aligned} \quad (6)$$

where g is the magnitude of the gravitational acceleration and G is the *grasp map* which is given by

$$G = \begin{bmatrix} Ad_{g_{oo}^{-1}}^T & Ad_{g_{ocl}^{-1}}^T B_{cl} & Ad_{g_{oo}^{-1}}^T & Ad_{g_{ocr}^{-1}}^T B_{cr} \end{bmatrix}, \quad (7)$$

where $Ad_{g_{ocl}^{-1}}^T$ and $Ad_{g_{ocr}^{-1}}^T$ transform the wrenches expressed in the contact frames \mathcal{C}_l and \mathcal{C}_r into ones expressed in the object frame \mathcal{O} ; $Ad_{g_{oo}^{-1}}^T$ transform the wrenches expressed in the object frame \mathcal{O} into ones expressed in the frame $\mathcal{O}[\mathcal{W}]$.

To relate the velocities of the object and the robot end-effectors, we have the so-called fundamental grasping constraint [30] which prescribes at the contact points, the velocities of the object and the end-effectors along the contact force directions should be equal, i.e.

$$J_a \dot{q} = G^T v_{\mathcal{O}} \quad \text{with} \quad v_{\mathcal{O}} = [{}^{\mathcal{W}}\dot{o}_{\mathcal{O}} \quad {}^{\mathcal{W}}\omega_{\mathcal{O}}^T]^T \in \mathbb{R}^6, \quad (8)$$

where $v_{\mathcal{O}}$ is usually called *hybrid* or *mixed* velocity of the object frame \mathcal{O} [31]. By differentiating the holonomic grasping constraint (8) with respect to time, we have

$$\dot{J}_a \dot{q} + J_a \ddot{q} - G^T \dot{v}_{\mathcal{O}} - \dot{G}^T v_{\mathcal{O}} = 0. \quad (9)$$

In this paper, we focus on devising analytic control laws that can achieve robust manipulation of the held object by means of guaranteeing contact stability.

III. CONTACT PARAMETRIZATION

Typically, a convenient strategy to handle constraints is to remove them by means of the parametrization technique. In brief, the procedure to apply the parametrization trick consists of the following steps: i) Transform the constrained design variables to unconstrained exogenous variables with a forward mapping Φ ; ii) Perform operations over the exogenous variables; iii) Project the resulting exogenous variables back to the design variables using an inverse mapping Φ^{-1} .

In the spirit of handling constraints through parametrization, we propose to parameterize the contact stability manifold with the help of a set of unconstrained exogenous variables to facilitate the subsequent design of contact-aware control laws. By doing so, the profile of the contact forces f will be expressed instead by the evolution of the exogenous variables ξ , whose corresponding contact force values will be guaranteed to lie within the contact friction cone \mathcal{FC} . In the following, we specifically illustrate the parametrization strategy for the unilateral planar contact model which appears as a quite representative contact type. Notably, the proposed parametrization strategy can be readily applied to other commonly encountered contact models, such as frictionless point contact, point contact with friction, and soft finger contact (see Fig. 3).

Formally, the contact stability constraints on the contact force brought by the unilateral planar contact model can be formulated as follows [32]:

$$f = \begin{bmatrix} f_x \\ f_y \\ f_z \\ M_x \\ M_y \\ M_z \end{bmatrix} \in \mathbb{R}^6 \quad \text{with} \quad \begin{cases} f_z > \delta > 0 & (10a) \\ \sqrt{f_x^2 + f_y^2} < \mu_c f_z & (10b) \\ -y_{\min} < -\frac{M_x}{f_z} < y_{\max} & (10c) \\ -x_{\min} < \frac{M_y}{f_z} < x_{\max} & (10d) \\ |M_z| < \mu_z f_z & (10e) \end{cases}$$

where x_{\max} , x_{\min} , y_{\min} , and y_{\max} represent the dimensions of the largest fitting rectangular inside the contact surface, δ is the normal force threshold, μ_c is the static friction coefficient and μ_z denotes the torsional friction coefficient. Our goal is to devise a contact wrench parametrization approach $\Phi(\xi) \in \mathbb{R}^6$ that maps free variable ξ to a valid unilateral planar contact wrench. Wherein, the free variable ξ is given as

$$\xi = [\xi_x \quad \xi_y \quad \xi_z \quad \xi_{M_x} \quad \xi_{M_y} \quad \xi_{M_z}]^T \in \mathbb{R}^6. \quad (11)$$

Property 1. In order to make the contact parametrization strategy $\Phi(\xi)$ a valid candidate, the following properties need to hold as pointed by [32]:

- The contact stability constraints (10) are satisfied for any value of ξ , i.e., $\Phi(\xi) \subset \mathcal{FC}$, $\forall \xi \in \mathbb{R}^6$.
- The mapping between the ξ -parametrized friction cone \mathcal{FC}_{ξ} and \mathbb{R}^6 is bijective.
- The gradient of the function $\Phi(\xi)$ is invertible.

In general, the form of the parametrization function $\Phi(\xi)$ is not unique. In this paper, we specifically consider the following parametrization approach.

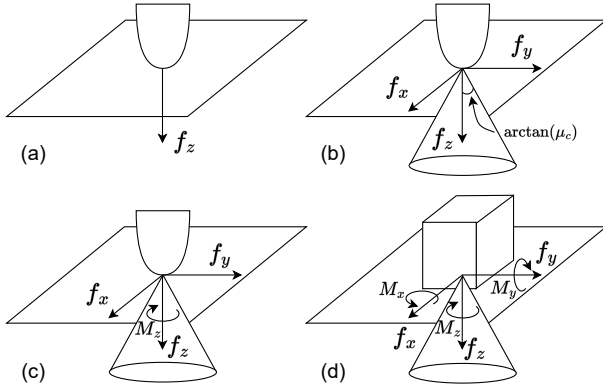


Fig. 3. Common contact models used for fixed-offset bimanual manipulation, namely (a) frictionless point contact, (b) point contact with friction, (c) soft finger, and (d) unilateral planar contact [30].

Proposition 1. Consider the following proposed parameterization method for the contact model (10):

$$\Phi(\xi) = \begin{bmatrix} \frac{\mu_c}{2}(\tanh(\xi_x)+1) \cos(\pi(\tanh(\xi_y)+1))(\exp(\xi_z)+\delta) \\ \frac{\mu_c}{2}(\tanh(\xi_x)+1) \sin(\pi(\tanh(\xi_y)+1))(\exp(\xi_z)+\delta) \\ \exp(\xi_z) + \delta \\ (\beta_y \tanh(\xi_{M_x}) + \delta_y)(\exp(\xi_z) + \delta) \\ (\beta_x \tanh(\xi_{M_y}) + \delta_x)(\exp(\xi_z) + \delta) \\ \mu_z \tanh(\xi_{M_z})(\exp(\xi_z) + \delta) \end{bmatrix} \quad (12)$$

where we define

$$\begin{aligned} \delta_x &= (x_{\max} - x_{\min})/2, & \beta_x &= -(x_{\min} + x_{\max})/2, \\ \delta_y &= (y_{\min} - y_{\max})/2, & \beta_y &= (y_{\min} + y_{\max})/2. \end{aligned} \quad (13)$$

The model (12) ensures that Property 1 holds.

Proof. Firstly note that our parametrization methods for f_x and f_y are distinguished from [32] while the parametrization of f_z , M_x , M_y , and M_z follows the same strategy. Therefore, our proof will focus solely on the parametrization methods for f_x and f_y and interested readers are referred to [32] for detailed proof of the properties for the remaining contact forces. To show that (12) is a valid candidate for contact parametrization, we need to prove that (12) satisfies the above listed three properties for contact parametrization.

For Property (a), our goal is to show that (10b) holds $\forall \xi_x, \xi_y, \xi_z \in \mathbb{R}$. To this end, we need to verify that

$$\sqrt{\Phi_1^2(\xi) + \Phi_2^2(\xi)} < \mu_c \Phi_3(\xi). \quad (14)$$

By substituting the corresponding parametrization expression into (14), we have

$$\sqrt{\frac{1}{4}(\tanh(\xi_x) + 1)^2} < 1, \quad (15)$$

where we drop out the positive terms from two sides of the equation and combine the equation with the Pythagorean identity. Finally, it can be verified that (15) holds given $\tanh(\xi_x) \in (-1, 1)$.

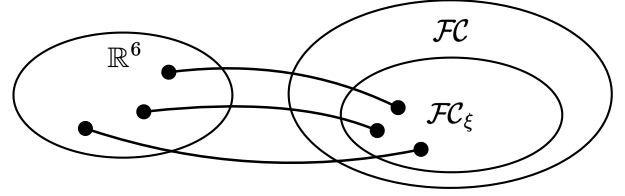


Fig. 4. Illustration of the set relation. The mapping between the free parameters and the parameterized contact stability manifold is bijective.

For Property (b), it can be firstly observed from (12) that a unique solution of f can be derived for any ξ . Then we can show that the inverse mapping $\Phi^{-1}(f)$ also returns a unique ξ given any $f \in \mathcal{FC}_\xi$. Specifically, ξ_x and ξ_y can be computed in terms of f . To yield the expression of ξ_x , we compute

$$f_x^2 + f_y^2 = \frac{1}{4}(\tanh(\xi_x) + 1)^2 f_z^2 \mu_c^2, \quad (16)$$

which gives the expression for ξ_x as

$$\xi_x = \operatorname{atanh}\left(2\sqrt{f_x^2 + f_y^2}/(f_z \mu_c) - 1\right). \quad (17)$$

For the calculation of ξ_y , we have that the following holds from the parametrization of f_x :

$$\cos(\pi(\tanh(\xi_y) + 1)) = 2f_x/(\mu_c f_z (\tanh(\xi_x) + 1)) \quad (18a)$$

$$= f_x/(\sqrt{f_x^2 + f_y^2}) \quad (18b)$$

where (18b) is obtained by substituting the expression of $\tanh(\xi_x) + 1$ from (16) into (18a). Hence, the expression for ξ_y can be calculated as

$$\xi_y = \begin{cases} \operatorname{atanh}\left(\frac{1}{\pi} \arccos\left(\frac{f_x}{\sqrt{f_x^2 + f_y^2}}\right) - 1\right), & f_y \geq 0 \\ \operatorname{atanh}\left(1 - \frac{1}{\pi} \arccos\left(\frac{f_x}{\sqrt{f_x^2 + f_y^2}}\right)\right), & f_y < 0, \end{cases} \quad (19a, 19b)$$

which reveals satisfaction of Property (b).

For Property (c), we will prove that $\nabla\Phi(\xi) \in \mathbb{R}^{6 \times 6}$ is invertible by its determinant being non-zero. The expression of $\nabla\Phi(\xi)$ can be directly computed from (12) as

$$\nabla\Phi(\xi) = \begin{bmatrix} \frac{\partial\Phi}{\partial\xi_x} & \frac{\partial\Phi}{\partial\xi_y} & \frac{\partial\Phi}{\partial\xi_z} & \frac{\partial\Phi}{\partial\xi_{M_x}} & \frac{\partial\Phi}{\partial\xi_{M_y}} & \frac{\partial\Phi}{\partial\xi_{M_z}} \end{bmatrix} \quad (21a)$$

$$= \begin{bmatrix} \nabla\Phi_{11} & \nabla\Phi_{12} & \nabla\Phi_{13} & 0 & 0 & 0 \\ \nabla\Phi_{21} & \nabla\Phi_{22} & \nabla\Phi_{23} & 0 & 0 & 0 \\ 0 & 0 & \nabla\Phi_{33} & 0 & 0 & 0 \\ 0 & 0 & \nabla\Phi_{43} & \nabla\Phi_{44} & 0 & 0 \\ 0 & 0 & \nabla\Phi_{53} & 0 & \nabla\Phi_{55} & 0 \\ 0 & 0 & \nabla\Phi_{63} & 0 & 0 & \nabla\Phi_{66} \end{bmatrix} \quad (21b)$$

The determinant of (21b) can be shown to be

$$\det(\nabla\Phi) = \nabla\Phi_{66} \nabla\Phi_{55} \nabla\Phi_{44} \nabla\Phi_{33} \begin{vmatrix} \nabla\Phi_{11} & \nabla\Phi_{12} \\ \nabla\Phi_{21} & \nabla\Phi_{22} \end{vmatrix} \quad (22)$$

where we have

$$\begin{vmatrix} \nabla\Phi_{11} & \nabla\Phi_{12} \\ \nabla\Phi_{21} & \nabla\Phi_{22} \end{vmatrix} = \nabla\Phi_{11} \nabla\Phi_{22} - \nabla\Phi_{12} \nabla\Phi_{21}. \quad (23)$$

$$\begin{aligned}
& \frac{\pi}{4}(1 - \tanh^2(\xi_x))(\tanh(\xi_x) + 1) \cos^2(\pi(\tanh(\xi_y) + 1)) (1 - \tanh^2(\xi_y))(\exp(\xi_z) + \delta)^2 \\
& + \frac{\pi}{4}(1 - \tanh^2(\xi_x))(\tanh(\xi_x) + 1) \sin^2(\pi(\tanh(\xi_y) + 1)) (1 - \tanh^2(\xi_y))(\exp(\xi_z) + \delta)^2 \\
& = \frac{\pi}{4}(1 - \tanh^2(\xi_x))(\tanh(\xi_x) + 1)(1 - \tanh^2(\xi_y))(\exp(\xi_z) + \delta)^2 > 0. \quad (20)
\end{aligned}$$

By employing the derivative of the tanh function, we can analytically expand (23) leading to (20), which is non-zero. ■

With the above results, we can conclude that the parametrization approach as given by (12) presents a valid contact parametrization. Nevertheless, it should be noted that the parametrized friction cone \mathcal{FC}_ξ with the proposed approach cannot completely cover the whole original friction cone \mathcal{FC} , i.e. $\mathcal{FC}_\xi \subset \mathcal{FC}$. For example, we can see from (19) that for the case $f_x = f_y = 0$, the numerator becomes zero, which will make the inverse mapping for ξ_y ill-posed. Practically, the situation of both f_x and f_y being zero at the same time will rarely happen, due to numerical errors, sensor noise, etc.

One salient merit of parametrizing f_x and f_y as (12) lies in that all elements within the friction cone (10b) can be covered except for the case of $f_x = f_y = 0$. By contrast, the parametrization strategy for f_x and f_y developed in [32] results in a set resembling an octagonal flipped pyramid, which covers only approximately 90% of the set prescribed by (10b). The set relations of the free-parameter space, the contact stability manifold with the proposed parametrization approach, and the original contact stability manifold are shown in Fig. 4.

The parameterization of other contact models follows a similar procedure to that of the unilateral planar contact as the conditions for these contact modeling can be shown to be a subset of (10).

IV. CONTROLLER DESIGN

In this section, we present the design of a controller that steers the object to move along a desired trajectory with the parametrization contact model.

A. Momentum Control with Contact Servoing

To control the momentum of the object, we design the control states as $s = [s_1^\top \ s_2^\top \ s_3^\top]^\top$, where each element is designed as

$$s_1 = \int_0^t \tilde{h} dt \quad (24a)$$

$$s_2 = \tilde{h} = \dot{s}_1 \quad (24b)$$

$$s_3 = K_p s_1 + K_d s_2 + \dot{s}_2 \quad (24c)$$

where the momentum error is defined as $\tilde{h} = h - h_d$, with h_d being the desired momentum value. In addition, we notice

$$\dot{s}_2 = \dot{\tilde{h}} = \dot{h} - \dot{h}_d = Gf_c - mge_3 - \dot{h}_d, \quad (25)$$

where s_1 represents the integral of the momentum error, s_2 represents the momentum error, and s_3 is an auxiliary state that

will facilitate independent control gain tuning of the closed-loop system dynamics as discussed in [33].

The dynamics of (24) can be written as

$$\dot{s}_1 = s_2 \quad (26a)$$

$$\dot{s}_2 = -K_p s_1 - K_d s_2 + s_3 \quad (26b)$$

$$\dot{s}_3 = -K_d K_p s_1 + (K_p - K_d^2) s_2 + K_d s_3 + u \quad (26c)$$

where \dot{s}_2 is chosen as the control signal as it contains the term of the contact change rate. Specifically, we have

$$u = \dot{s}_2 = \dot{G}f_c + G\dot{f}_c - \dot{h}_d \quad (27a)$$

$$= \dot{G}f_c + G\nabla\Phi(\xi)\dot{\xi} - \dot{h}_d. \quad (27b)$$

As an abuse of notation, we have $\xi = [\xi_l^\top \ \xi_r^\top]^\top$ with $\xi_l \in \mathbb{R}^{ncl}$ and $\xi_r \in \mathbb{R}^{ncr}$. Besides, $\Phi(\xi) = [\Phi_l(\xi_l)^\top \ \Phi_r(\xi_r)^\top]^\top$ with f_l and f_r parametrized by Φ_l and Φ_r , respectively. In accordance, we have

$$\nabla\Phi(\xi) = \begin{bmatrix} \nabla\Phi_l(\xi_l) & 0_{ncl \times ncr} \\ 0_{ncr \times ncl} & \nabla\Phi_r(\xi_r) \end{bmatrix}. \quad (28)$$

The temporal derivative of the grasp map in (27) is derived as

$$\dot{G} = \left[\frac{d}{dt} (Ad_{g_{woo}}^\top) Ad_{g_{ocl}}^\top B_{cl} \quad \frac{d}{dt} (Ad_{g_{woo}}^\top) Ad_{g_{ocr}}^\top B_{cr} \right] \quad (29a)$$

$$\text{where } \frac{d}{dt} (Ad_{g_{woo}}^\top) = -Ad_{g_{woo}}^\top \dot{a} d_{g^{-1}\dot{g}} \quad (29b)$$

The behavior of the dynamic system can be written in the state-space model form as

$$\begin{bmatrix} \dot{s}_1 \\ \dot{s}_2 \\ \dot{s}_3 \end{bmatrix} = \begin{bmatrix} 0 & \mathbf{1} & 0 \\ -K_p & -K_d & \mathbf{1} \\ -K_d K_p & K_p - K_d^2 & K_d \end{bmatrix} \begin{bmatrix} s_1 \\ s_2 \\ s_3 \end{bmatrix} + \begin{bmatrix} 0 \\ 0 \\ \mathbf{1} \end{bmatrix} u \quad (30)$$

Our control objective is *output regulation*, namely, designing the control law u such that the output of the closed-loop system s converges to zero. To this end, we consider employing the linear state feedback control strategy parametrized in the following form:

$$u = K_1 s_1 + K_2 s_2 + K_3 s_3, \quad (32)$$

where K_1 , K_2 , and K_3 denote the state feedback gain matrices. As a result, the system dynamics (30) upon integrating the control law (32) becomes

$$\begin{bmatrix} \dot{s}_1 \\ \dot{s}_2 \\ \dot{s}_3 \end{bmatrix} = \begin{bmatrix} 0 & \mathbf{1} & 0 \\ -K_p & -K_d & \mathbf{1} \\ K_1 - K_d K_p & K_2 + K_p - K_d^2 & K_3 + K_d \end{bmatrix} \begin{bmatrix} s_1 \\ s_2 \\ s_3 \end{bmatrix} \quad (33)$$

which can be compactly denoted as an autonomous system: $\dot{s} = A_u s$. Recall that to ensure asymptotic stability of linear state space model (33), all real parts of the eigenvalues of A_u

$$A_u^\top V + V A_u = \begin{bmatrix} 0 & V_1 - K_p V_2 & (K_1 - K_p K_d) V_3 \\ V_1 - V_2 K_p & -K_d V_2 - V_2 K_d & (K_2 + K_p - K_d^2) V_3 + V_2 \\ V_3 (K_1 - K_d K_p) & V_3 (K_2 + K_p - K_d^2) + V_2 & V_3 (K_3 + K_d) + (K_3 + K_d) V_3 \end{bmatrix} \quad (31)$$

should be negative. Alternatively, this condition is equivalent to satisfying the following Lyapunov matrix equation:

$$A_u^\top V + V A_u \prec 0 \quad (34)$$

where V is some symmetric positive definite matrix. Let us choose V in the following form for simplicity:

$$V = V_1 \oplus V_2 \oplus V_3, \quad (35)$$

where \oplus represents the matrix direct sum, and V_1 , V_2 , and V_3 are symmetric positive definite matrices. By substituting (35) into (34), we have the expression for $A_u^\top V + V A_u$ as (31).

To make (31) a negative definite matrix, we specifically choose the following control feedback matrices:

$$K_1 = K_d K_p \quad (36a)$$

$$K_2 = K_d^2 - K_p - V_3^{-1} \quad (36b)$$

$$K_3 = -K_d - \mathbf{1} \quad (36c)$$

In addition, we choose $V_1 = K_p$ and $V_2 = \mathbf{1}$ without loss of stability guarantee, which yields (31) as

$$A_u^\top V + V A_u = -2(0_{6 \times 6} \oplus K_d \oplus V_3) \quad (37)$$

Notice, however, that (37) is a negative semi-definite matrix, from which the stability of (32) can not be concluded in general. Nevertheless, by checking the Lyapunov function candidate $s^\top V s$ and invoking the LaSalle's invariance principle, the asymptotic stability of the equilibrium point $s = 0$ can be obtained. More detailed discussion can be found in [33].

Consequently, using the feedback gains given as (36), the control law becomes

$$u = K_p K_d s_1 + (K_d^2 - K_p - V_3^{-1}) s_2 - (K_d + \mathbf{1}) s_3. \quad (38)$$

B. Pose and Postural Control

In order to control the pose and its velocities of the object, we consider the control laws by explicitly instantiating the components s_1 , s_2 , and s_3 .

For the design of s_2 , we have

$$s_2 = \begin{bmatrix} m_{\mathcal{O}}(\mathcal{W}_{\mathcal{O}} - \dot{p}_d) \\ \mathcal{O}^{[\mathcal{W}]} I(\mathcal{W}_{\mathcal{O}} - \omega_d) \end{bmatrix} \quad (39)$$

where \dot{p}_d and ω_d represent the desired linear and angular velocity, respectively.

For the control of the pose, we consider the design of the integral term s_1 as

$$s_1 = \begin{bmatrix} P(0) + \int_0^t \tilde{P}(t) dt \\ L(0) + \int_0^t \tilde{L}(t) dt \end{bmatrix} = \begin{bmatrix} m_{\mathcal{O}}(\mathcal{W}_{\mathcal{O}} - p_d) \\ \mathcal{O}^{[\mathcal{W}]} I(S(\mathcal{W}_{R_{\mathcal{O}}} R_d^\top))^\vee \end{bmatrix} \quad (40)$$

where $P(0)$ and $L(0)$ denote the integral initial conditions.

The design of auxiliary state variable s_3 then follows from its definition (24c) directly.

For the virtual control inputs $\dot{\xi}$, we equate (27) and (38):

$$\dot{\xi} = (G\nabla\Phi(\xi))^\dagger (K_p K_d s_1 + (K_d^2 - K_p - V_3^{-1}) s_2 - (K_d + \mathbf{1}) s_3 - \dot{G} f_c + \ddot{h}_d) + \dot{\xi}_N, \quad (41)$$

where we additionally append $\dot{\xi}_N$ to $\dot{\xi}$ to exploit the null space of $G\nabla\Phi(\xi)$. We choose $\dot{\xi}_N$ in a way such that the contact model tends to the desired contact configuration ξ_d , namely

$$\dot{\xi}_N = \mathcal{N}(G\nabla\Phi(\xi))(-K_\xi(\xi - \xi_d)), \quad (42)$$

where K_ξ denotes a symmetric positive definite matrix.

To realize the execution of $\dot{\xi}$ by the bimanual robots, we provide two strategies, namely admittance control and torque control. For the admittance control which takes measured force as the input and outputs robot position, we provide the admittance model with

$$f_c(\dot{\xi}) = \Phi \left(\Phi^{-1}(f_c(0)) + \int_0^t \dot{\xi} dt \right), \quad (43)$$

where the initial condition $\xi(0) = \Phi^{-1}(f_c(0))$ is read from the F/T sensors.

To realize the execution of $\dot{\xi}$ by joint torques, the relationship between τ and $\dot{\xi}$ can be found out by cancelling out \ddot{q} from (1) using (9):

$$\dot{J}_a \dot{q} + J_a M_a^{-1}(\tau + J_a^\top f_c - C_a \dot{q} - g_a) - G^\top \dot{v}_{\mathcal{O}} - \dot{G}^\top v_{\mathcal{O}} = 0. \quad (44)$$

Consequently, the computation of dual-arm joint torques can be derived from (44) as

$$\tau(\dot{\xi}) = (J_a M_a^{-1})^\dagger (G^\top \dot{v}_{\mathcal{O}} + \dot{G}^\top v_{\mathcal{O}} - \dot{J}_a \dot{q}) - J_a^\top f_c(\dot{\xi}) + C_a \dot{q} + g_a + \tau_N \quad (45)$$

Furthermore, to guarantee the stability of the system *zero dynamics*, i.e. the evolution of system (1) at $s = 0$ in the case of the presence of joint redundancy (i.e. n_l and $n_r > 6$), a joint-space postural task can be incorporated to handle this redundancy [34]. Given a reference position for the joint configuration as q_d , the null-space joint torque is given as:

$$\tau_N = \mathcal{N}(J_a M_a^{-1})(-K_q(q - q_d)) \quad (46)$$

where K_q denotes a symmetric positive definite matrix.

V. RESULTS

In this section, we report the results from both simulation and experimental studies to illustrate the effectiveness of our proposed approach.

A. Comparisons

In this part, we compare our approach with the baseline method by [32]. We first compare the morphology of the friction cones parametrized by both approaches. The minimum normal force f_z of the friction cone is set to be $\delta = 0.01$ N and the maximum normal force, which determines the height of the friction cone, is selected by setting $\xi_z = 1$, leading to the maximum normal force being 2.7 N. In addition, the friction coefficient is chosen as $\mu_c = 0.5$. It can be seen in Fig. 5 that both approaches can satisfy the constraint of the friction cone given any values of the corresponding exogenous parameters. Moreover, the cross-section of the friction cone parametrized by the baseline approach resembles an octagon, which implies that around 10% of the original friction cone cannot be covered. As a comparison, our approach possesses the merit of parametrizing more regions of the friction cone as evidenced by the shape of its cross section.

B. Simulations

In this section, we evaluate the contact force tracking behavior based on our proposed contact parametrization model with simulation studies. We first compare the friction forces tracking performance with the baseline method. Specifically, we design the reference friction profiles with the maximum allowable friction magnitude 5 N and they are given by $f_x = 5 \sin(\pi(t + 0.5))$ N and $f_y = 5 \cos(\pi(t + 0.5))$ N. The start point for both approaches is set to be $f_{x0} = 0$ N and $f_{y0} = -1$ N. The tracking performance is shown in Fig. 6. It can be observed that our method achieves a higher tracking precision compared with the baseline method. Besides, the tracking profile with our approach is shown to be smoother. The baseline method is observed to periodically exhibit small spikes, which represents an inherent issue brought by the parametrization strategy.

We then compare our approach with the control strategy of fixed-distance-penetration grasping in terms of object motion control. Specifically, we consider the orientation tracking task, where we let the robot arms rotate around the z -axis of the contact frames. In this task, we are particularly concerned with the model of (10e). We would like to rotate an object that has unit inertia around the z -axis of the contact frames to track a constant angular acceleration 0.6 rad s^{-2} from at rest. The torsional friction coefficient is chosen to be $\mu_z = 0.1$ and the normal contact force between the object and one of the end-effectors is set to be a constant of 2.5 N, which can provide a maximum angular acceleration of 0.5 rad s^{-2} . When using our approach, the angular acceleration of the object reaches the maximum allowable value without violating it, as seen in Fig. 7. For comparison, we employ the control strategy of fixed-distance penetration where the constant normal force is also 2.5 N and the end-effectors rotate based on the angular acceleration reference. In this case, there is a slip between the object and the end-effectors as the maximum allowable moment is insufficient to track the given reference profile.

For another evaluation, we chose the ball-lifting task, where the contact model corresponds to the model of point contact with friction. The unit-weight ball is lifted upwards from at

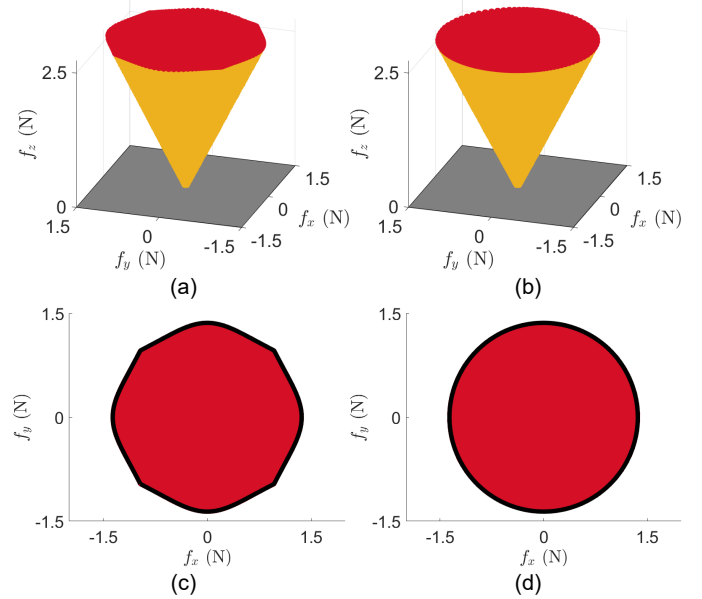


Fig. 5. Comparison of the parametrization performance by (a) the baseline approach and (b) our approach as well as the cross-section shape of the parametrized friction cone by (c) the baseline approach and (d) our approach.

rest by dual arms with a reference of linear growing acceleration $t + 0.3 \text{ m s}^{-2}$ at a direction opposite to the gravity. The normal force between one arm and the ball is set to be 10 N and the friction coefficient $\mu_c = 0.55$, which leads the maximum allowable acceleration to be 1 m s^{-2} . The tracking results are shown in Fig. 7. When using our approach, the acceleration of the ball is saturated at the maximum value, resulting in robust grasping. By contrast, when controlling the ball using the fixed-distance penetration with the same contact force and the end-effectors moving according to the reference acceleration, the contact is broken at 0.68 s and the ball falls from the dual arms immediately afterward.

C. Experiments

To validate our proposed approach, we perform experimental studies with a dual-arm robotic system, which is composed of two identical six-DoF UR3 robot manipulators positioned 0.75 m away from each other. Each end-effector is equipped with a Robotiq FT-300 F/T sensor. Besides, an Intel Realsense L515 camera, which has a resolution of 1280×780 , is mounted to sense the top-down view of the manipulation space. The coordinate transformation between the depth camera and both arms is calibrated through the markers. The position of the box is localized via the ArUco markers attached to the center of the box surfaces. The axes of the ArUco markers are aligned with the sides of the box. An illustration of the employed experimental set-up is shown in Fig. 1.

The length, width, and height of the manipulated box is $200 \text{ mm} \times 130 \text{ mm} \times 140 \text{ mm}$. The weight of the box is 150 g and is assumed to be uniformly distributed. The customized end-effectors possess a rectangular shape with a length of 10 cm and a width of 6 cm. We position the origin of the contact frames at the center of the end-effectors, leading

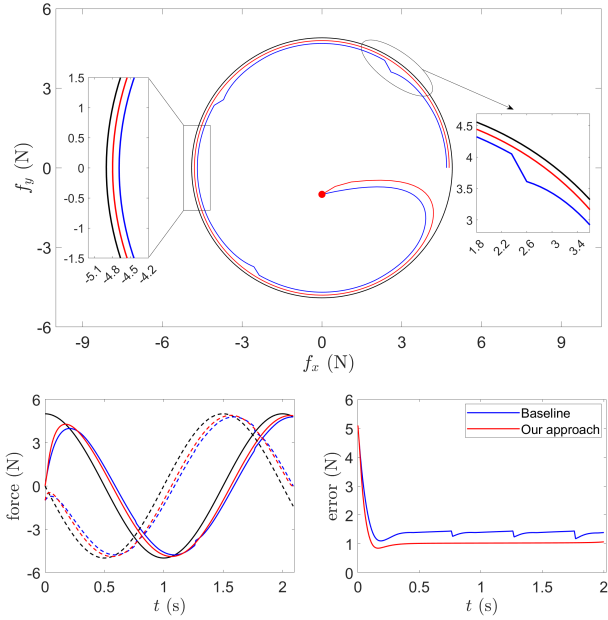


Fig. 6. Comparison of tracking friction reference (black) with baseline (blue) and our approach (red). The start point is marked with a red dot.

to $x_{\min} = -0.05$ m, $x_{\max} = 0.05$ m, $y_{\min} = -0.03$ m, and $y_{\max} = 0.03$ m for the left contact. The contact dimension parameters for the right contact can also be obtained accordingly. Moreover, the static friction coefficient between the object and the box is $\mu_c = 0.5$.

The effectiveness of the proposed approach is validated through three representative bimanual manipulation tasks, namely the linear transportation task, the circular movement task, and the object shaking task. Our goal is to showcase that the trajectories of the center of the box can be steered to track these specified reference trajectories of different tasks by means of robust dual-arm manipulation. Also, we would like to have the normal contact force between the box and the robot end-effectors to track a desired force profile.

It should be noted when joint torque control is not available as in our case, the virtual control input (41) is thus considered to be realized with an admittance control strategy to generate joint position commands for the robot arms. The schematic diagram of the control block to perform the transportation tasks is illustrated in Fig. 8. It mainly consists of three parts, namely the robot commands generator, the robot system, and the contact stabilizer. The robot commands generator is exactly the admittance controller, responsible for sending the joint position reference to the position-controlled robots. The robot system then manipulates the object by executing the received control signals. The contact stabilizer takes the object's states and the desired object motion as input and then sends the contact wrench as specified by (43) to the admittance controller.

For the task of linear transportation, our goal is to control the motion of the box such that its center tracks a desired trajectory. The desired trajectory is designed to be a straight line in the operational space and its expression with respect to time t is given by

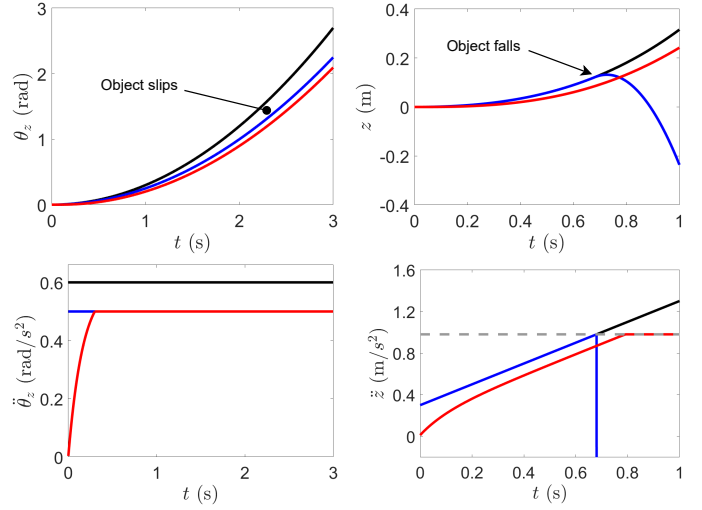


Fig. 7. Illustration of object trajectory in the orientation tracking task (left column) and the ball lifting task (right column) using our approach (red) and fixed-distance penetration (blue) in response to a given reference (black).

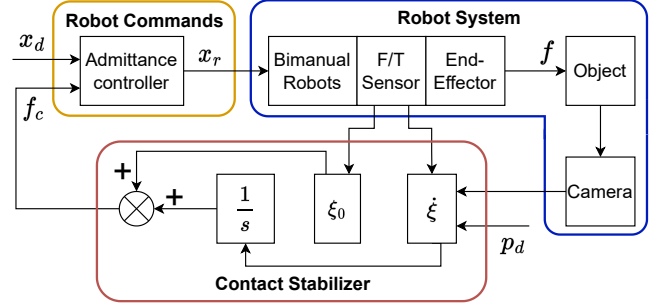


Fig. 8. Schematic diagram of the control block.

$$p_d(t) = (0.014t - 0.41)e_1 - 0.25e_2 + (0.022t + 0.15)e_3$$

where the time duration is $t \in [0, 5]$ s. The initial position of the box with respect to the base frame of the left arm is set to be $[-0.35, -0.25, 0.25]^T$ m. And the final position to reach is set to be $p_d(5) = [-0.34, -0.25, 0.26]^T$ m.

During the linear transportation task, the box remains in a constant rotation configuration. Specifically, the orientation of the box is controlled in a way such that it keeps the same as that of the left arm base frame. For the normal force of the initial contact wrench, it is set to be 2.2 N for both arms. Specifically, the corresponding free parameter for f_z is then initialized as $\xi_{0z} = -0.357$, provided that the normal force threshold is $\delta = 1.5$ N. The normal contact force profile is set as a constant of 5 N. The illustration of tracking performance for the linear transportation task is shown in Fig. 9. Both movement of the box along both x - and z -axis can track the desired given linear reference, as seen by the evolution of the error profile converging to zero. Also, the normal contact force is able to track the desired constant force profile.

For the task of circular movement, our goal is to control the motion of the box such that its center can track a given circular trajectory. The initial position of the box is

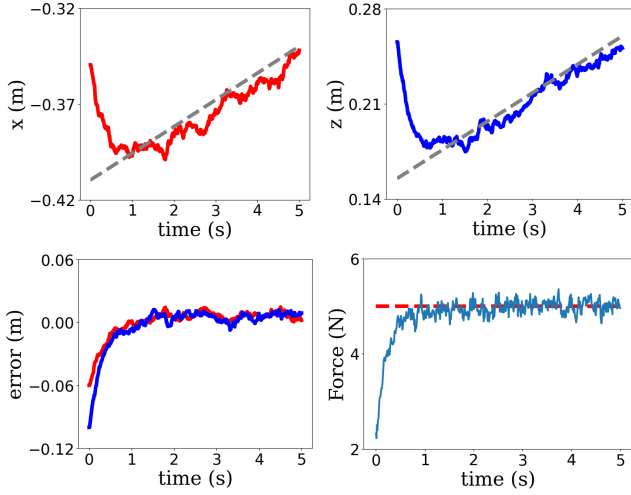


Fig. 9. Illustration of the left end-effector motion along the x -axis (*upper left*), the z -axis (*upper right*), error evolution (*lower left*), and force tracking (*lower right*) in the linear transportation task, where the grey-dashed line is the motion reference and the red-dashed is the force reference.

at $[-0.35, -0.25, 0.5]^T$ m with respect to the left arm-based frame. The expression for the circular reference trajectory with a period of 6 s is designed to be

$$p_d(t) = \left(0.1 \sin\left(\frac{\pi}{3}t\right) - 0.26\right) e_1 - 0.25e_2 \\ \left(0.11 \sin\left(\frac{\pi}{3}(t + 1.5)\right) + 0.35\right) e_3$$

where we have $t \in [0, 9]$ s.

The orientation of the box is controlled to be the same as that of the left arm base frame. The z -component of the initial contact wrench for this task is set to be 6 N, which corresponds to $\xi_{0z} = 1.5$. The desired normal contact force in this task is set to be 9 N. The box is then transported by the dual arms for 9 s, which accounts for one and a half circles in the operational space. The illustration of tracking performance for the circular movement task is shown in Fig. 10. It can be seen that overall the box can track the specified position trajectory along the x - and z -axis. In this case, the error evolution also exhibits periodicity, which is a result of the temporal delays in the periodic tracking task.

For the task of object shaking, we would like the robot to move the box up and down along the z -axis. The reference trajectory, in this case, is given by integrating the following piece-wise constant velocity trajectory

$$\dot{p}_d(t) = \begin{cases} -0.92e_3, & \text{if } \text{int}(t/0.26) \text{ is even,} \\ 0.92e_3, & \text{otherwise} \end{cases}$$

where we have $t \in [0, 5]$ s. The resulting jagged reference trajectory at the position level will require the box to frequently switch between moving upwards and moving downwards. Particularly, we specify the duration for one-way movement to be 0.26 s, which will make the robot shake the box approximately twice in one second. The highest point that the box can reach in z -direction is 0.32 m and the lowest point is 0.27 m, which leads the shaking magnitude to be 0.05 m. The illustration of tracking performance for the shaking task is shown in Fig. 11.

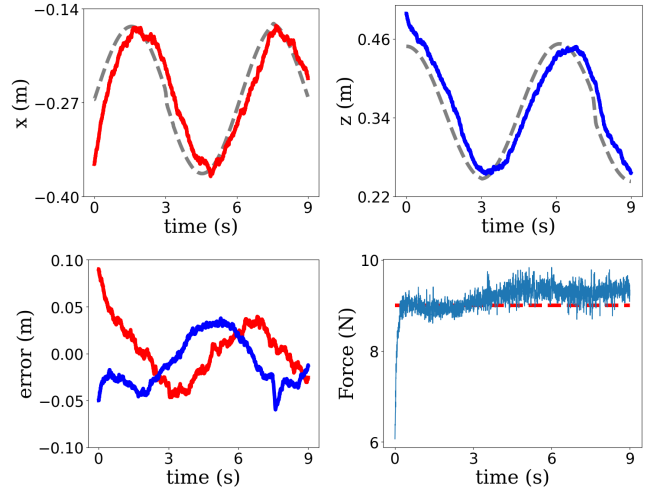


Fig. 10. Illustration of the left end-effector motion along the x -axis (*upper left*), the z -axis (*upper right*), error evolution (*lower left*), and force tracking (*lower right*) in the circular transportation task, where the grey-dashed line is the motion reference and the red-dashed is the force reference.

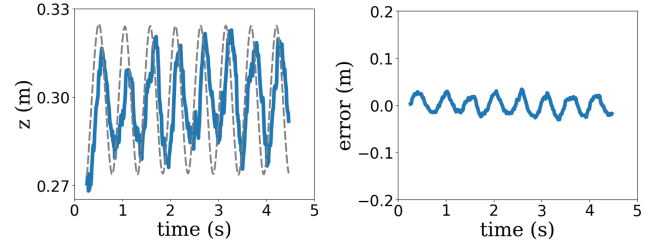


Fig. 11. Illustration of the left end-effector motion along the z -axis (*left*) and error evolution (*right*) in the shaking task, where the grey-dashed line is the motion reference.

We can see that the tracking performance in this task exhibits more apparent delays due to the frequent direction change of the reference.

The snapshots of the experimental procedure for the aforementioned bimanual manipulation tasks are illustrated in Fig. 12, where we use the red curves to denote the direction of motion of the manipulated object.

To better illustrate the superiority of the proposed approach, we compare our control approach with a baseline controller. When performing bimanual grasping of the box with the employed baseline controller, the end-effectors keep a fixed relative distance that is slightly smaller than the width of the box. The contact between the end-effector and the box is only established due to the slight penetration into the box and consequently, there is no force feedback information from the F/T sensors taken into account.

It is observed that the success rate of the proposed approach is higher than that of the baseline controller. The most remarkable difference happens for the shaking task. The dual-arm robotic system with the proposed approach can successfully perform the shaking task for nine out of ten trials. The failure trial could be caused by a few factors, such as F/T sensor noises, marker tracking issues, matrix inversion errors, etc. By contrast, the performance of the baseline controller degrades

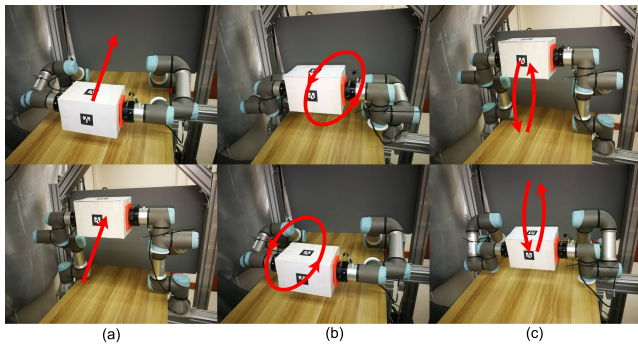


Fig. 12. Snapshots of the procedure for performing (a) linear transportation task where the box is moved along an inclined line, (b) circular movement task where the box is moved periodically along a circle, and (c) object shaking task where the box is shaken upwards and downwards. The red arrow curves denote the moving directions of the box.

dramatically with a success rate of only two out of ten. Typically, such highly dynamic tasks require explicitly maintaining the interaction forces, which highlights the significance of the proposed robust bimanual grasping control strategy.

VI. CONCLUSION

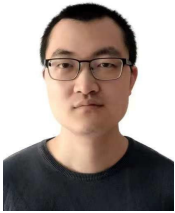
In this paper, we presented a bimanual manipulation control strategy for fixed-offset object transportation. In particular, our proposed approach focuses on guaranteeing the stability of the contact by a parametrization model. Subsequently, such a contact model is exploited such that trajectory tracking can be achieved for the held object. The effectiveness of the proposed approach is well verified with both simulation studies and real experiments of box transportation tasks.

For limitations, at the moment, our controller assumes that the mass and the inertia tensor of the object are known a priori. Such an assumption would prohibit the robot system from transporting objects with unknown dynamic properties. An estimation algorithm could be integrated into our control framework such that the bimanual robotic system is able to handle unknown-weight payload [35]. For future work, it is also interesting to incorporate obstacle avoidance into the current framework [36].

REFERENCES

- [1] C. Smith, Y. Karayiannidis, L. Nalpantidis, X. Gratal, P. Qi, D. V. Dimarogonas, and D. Kragic, "Dual arm manipulation—a survey," *Robotics and Autonomous systems*, vol. 60, no. 10, pp. 1340–1353, 2012.
- [2] J. Huo, A. Duan, C. Li, P. Zhou, W. Ma, H. Wang, and D. Navarro-Alarcon, "Keypoint-based planar bimanual shaping of deformable linear objects under environmental constraints with hierarchical action framework," *IEEE Robotics and Automation Letters*, vol. 7, no. 2, pp. 5222–5229, 2022.
- [3] J. Qi, G. Ma, J. Zhu, P. Zhou, Y. Lyu, H. Zhang, and D. Navarro-Alarcon, "Contour moments based manipulation of composite rigid-deformable objects with finite time model estimation and shape/position control," *IEEE/ASME Transactions on Mechatronics*, 2021.
- [4] P. Zhou, J. Zhu, S. Huo, and D. Navarro-Alarcon, "LaSeSOM: A latent and semantic representation framework for soft object manipulation," *IEEE Robotics and Automation Letters*, vol. 6, no. 3, pp. 5381–5388, 2021.
- [5] J. Liu, Y. Chen, Z. Dong, S. Wang, S. Calinon, M. Li, and F. Chen, "Robot cooking with stir-fry: Bimanual non-prehensile manipulation of semi-fluid objects," *IEEE Robotics and Automation Letters*, vol. 7, no. 2, pp. 5159–5166, 2022.
- [6] J. Zhu, B. Navarro, P. Fraise, A. Crosnier, and A. Cherubini, "Dual-arm robotic manipulation of flexible cables," in *2018 IEEE/RSJ International Conference on Intelligent Robots and Systems (IROS)*. IEEE, 2018, pp. 479–484.
- [7] J. Silvério, L. Rozo, S. Calinon, and D. G. Caldwell, "Learning bimanual end-effector poses from demonstrations using task-parameterized dynamical systems," in *IEEE/RSJ international conference on intelligent robots and systems (IROS)*. IEEE, 2015, pp. 464–470.
- [8] A. Colomé and C. Torras, "Dimensionality reduction for dynamic movement primitives and application to bimanual manipulation of clothes," *IEEE Transactions on Robotics*, vol. 34, no. 3, pp. 602–615, 2018.
- [9] K. Yao, D. Sternad, and A. Billard, "Hand pose selection in a bimanual fine-manipulation task," *Journal of Neurophysiology*, vol. 126, no. 1, pp. 195–212, 2021.
- [10] S. Cruciani, D. Almeida, D. Kragic, and Y. Karayiannidis, "Discrete bimanual manipulation for wrench balancing," in *2020 IEEE International Conference on Robotics and Automation (ICRA)*. IEEE, 2020, pp. 2631–2637.
- [11] D. Rakita, B. Mutlu, M. Gleicher, and L. M. Hiatt, "Shared control-based bimanual robot manipulation," *Science Robotics*, vol. 4, no. 30, p. eaaw0955, 2019.
- [12] L. Rapetti, Y. Tirupachuri, A. Ranavolo, T. Kawakami, T. Yoshiike, and D. Pucci, "Shared control of robot-robot collaborative lifting with agent postural and force ergonomic optimization," in *2021 IEEE International Conference on Robotics and Automation (ICRA)*, 2021, pp. 9840–9847.
- [13] S. S. Mirrazavi Salehian, N. Figueroa, and A. Billard, "A unified framework for coordinated multi-arm motion planning," *The International Journal of Robotics Research*, vol. 37, no. 10, pp. 1205–1232, 2018.
- [14] J. Silvério, S. Calinon, L. Rozo, and D. G. Caldwell, "Bimanual skill learning with pose and joint space constraints," in *2018 IEEE-RAS 18th International Conference on Humanoid Robots (Humanoids)*. IEEE, 2018, pp. 153–159.
- [15] Z. Dong, Z. Li, Y. Yan, S. Calinon, and F. Chen, "Passive bimanual skills learning from demonstration with motion graph attention networks," *IEEE Robotics and Automation Letters*, vol. 7, no. 2, pp. 4917–4923, 2022.
- [16] O. Zahra, S. Tolu, P. Zhou, A. Duan, and D. Navarro-Alarcon, "A bio-inspired mechanism for learning robot motion from mirrored human demonstrations," *Frontiers in Neurorobotics*, vol. 16, 2022.
- [17] I. Kao, K. M. Lynch, and J. W. Burdick, "Contact modeling and manipulation," in *Springer Handbook of Robotics*. Springer, 2016, pp. 931–954.
- [18] Y. Nakamura, *Advanced robotics: redundancy and optimization*. Addison-Wesley Longman Publishing Co., Inc., 1990.
- [19] Q. Sun, "Control of flexible-link multiple manipulators," *J. Dyn. Sys., Meas., Control*, vol. 124, no. 1, pp. 67–75, 2002.
- [20] H. Audren and A. Kheddar, "3-D robust stability polyhedron in multi-contact," *IEEE Transactions on Robotics*, vol. 34, no. 2, pp. 388–403, 2018.
- [21] S. Caron, Q.-C. Pham, and Y. Nakamura, "Stability of surface contacts for humanoid robots: Closed-form formulae of the contact wrench cone for rectangular support areas," in *2015 IEEE International Conference on Robotics and Automation (ICRA)*. IEEE, 2015, pp. 5107–5112.
- [22] B. Aceituno-Cabezas, C. Mastalli, H. Dai, M. Focchi, A. Radulescu, D. G. Caldwell, J. Cappelletto, J. C. Grieco, G. Fernández-López, and C. Semini, "Simultaneous contact, gait, and motion planning for robust multilegged locomotion via mixed-integer convex optimization," *IEEE Robotics and Automation Letters*, vol. 3, no. 3, pp. 2531–2538, 2017.
- [23] S. Dafarra, G. Romualdi, G. Metta, and D. Pucci, "Whole-body walking generation using contact parametrization: A non-linear trajectory optimization approach," in *2020 IEEE International Conference on Robotics and Automation (ICRA)*. IEEE, 2020, pp. 1511–1517.
- [24] A. Duan, R. Camoriano, D. Ferigo, D. Calandriello, L. Rosasco, and D. Pucci, "Constrained DMPs for feasible skill learning on humanoid robots," in *2018 IEEE-RAS 18th International Conference on Humanoid Robots (Humanoids)*. IEEE, 2018, pp. 1–6.
- [25] L. Yan, Y. Yang, W. Xu, and S. Vijayakumar, "Dual-arm coordinated motion planning and compliance control for capturing moving objects with large momentum," in *2018 IEEE/RSJ International Conference on Intelligent Robots and Systems (IROS)*. IEEE, 2018, pp. 7137–7144.
- [26] J. Gao, Y. Zhou, and T. Asfour, "Projected force-admittance control for compliant bimanual tasks," in *2018 IEEE-RAS 18th International Conference on Humanoid Robots (Humanoids)*. IEEE, 2018, pp. 1–9.
- [27] Y. Jiang, Y. Wang, Z. Miao, J. Na, Z. Zhao, and C. Yang, "Composite-learning-based adaptive neural control for dual-arm robots with relative motion," *IEEE Transactions on Neural Networks and Learning Systems*, 2020.

- [28] F. Xie, A. Chowdhury, M. De Paolis Kaluza, L. Zhao, L. Wong, and R. Yu, "Deep imitation learning for bimanual robotic manipulation," *Advances in Neural Information Processing Systems*, vol. 33, pp. 2327–2337, 2020.
- [29] C. Yang, Y. Jiang, J. Na, Z. Li, L. Cheng, and C.-Y. Su, "Finite-time convergence adaptive fuzzy control for dual-arm robot with unknown kinematics and dynamics," *IEEE Transactions on Fuzzy Systems*, vol. 27, no. 3, pp. 574–588, 2019.
- [30] R. M. Murray, Z. Li, and S. S. Sastry, *A mathematical introduction to robotic manipulation*. CRC press, 2017.
- [31] S. Traversaro, "Modelling, Estimation and Identification of Humanoid Robots Dynamics," Ph.D. dissertation, University of Genoa, Apr. 2017. [Online]. Available: <https://doi.org/10.5281/zenodo.3564797>
- [32] A. Gazar*, G. Nava*, F. J. A. Chavez, and D. Pucci, "Jerk control of floating base systems with contact-stable parameterized force feedback," *IEEE Transactions on Robotics*, vol. 37, no. 1, pp. 1–15, 2020.
- [33] D. Pucci, S. Traversaro, and F. Nori, "Momentum control of an underactuated flying humanoid robot," *IEEE Robotics and Automation Letters*, vol. 3, no. 1, pp. 195–202, 2017.
- [34] A. Duan, R. Camoriano, D. Ferigo, Y. Huang, D. Calandriello, L. Rosasco, and D. Pucci, "Learning to sequence multiple tasks with competing constraints," in *2019 IEEE/RSJ International Conference on Intelligent Robots and Systems (IROS)*, 2019, pp. 2672–2678.
- [35] L. Han, W. Xu, B. Li, and P. Kang, "Collision detection and coordinated compliance control for a dual-arm robot without force/torque sensing based on momentum observer," *IEEE/ASME Transactions on Mechatronics*, vol. 24, no. 5, pp. 2261–2272, 2019.
- [36] A. Duan, R. Camoriano, D. Ferigo, Y. Huang, D. Calandriello, L. Rosasco, and D. Pucci, "Learning to avoid obstacles with minimal intervention control," *Frontiers in Robotics and AI*, vol. 7, p. 60, 2020.



Anqing Duan received his bachelor's degree in mechanical engineering from Harbin Institute of Technology, Harbin, China, in 2015, his master's degree in mechatronics from KTH, Sweden, in 2017, and his Ph.D. degree in robotics from the Istituto Italiano di Tecnologia and the Università degli Studi di Genova, Italy, in 2021. Since 2021, he has been a Research Associate with The Hong Kong Polytechnic University. His current research interests include machine learning and control systems focusing on robotic applications.



Shengzeng Huo received the B.S. degree in vehicle engineering from the South China University of Technology, Guangzhou, China, in 2019. He is currently pursuing the Ph.D. degree in the Department of Mechanical Engineering from The Hong Kong Polytechnic University, Hong Kong. His research interests include bimanual manipulation, deformable object manipulation, and robot learning.



Hoi-Yin Lee received the B.Eng. degree in Mechanical Engineering from The Hong Kong Polytechnic University of Hong Kong (PolyU), Kowloon, Hong Kong, in 2021.

She is currently pursuing the Ph.D. degree in Mechanical Engineering at the PolyU. Her research interests include multi-robot systems, perceptual robots, image processing, and automation.



Peng Zhou received the M.Sc. degree in software engineering from Tongji University, Shanghai, China, in 2017. Since 2019, he is pursuing his Ph.D. degree in robotics at The Hong Kong Polytechnic University, Kowloon, Hong Kong SAR, China. In 2021, he was a visiting Ph.D. student at Robotics, Perception and Learning Lab, KTH Royal Institute of Technology, Stockholm, Sweden. His research interests include deformable object manipulation, robot learning, and interactive perception.



CONTROL AND SIGNAL PROCESSING.

Jose Guadalupe Romero (Member, IEEE) obtained the Ph.D. degree in Control Theory from the University of Paris-Sud XI, France in 2013. Currently, he is the Chair of the Department of Electrical and Electronic Engineering at ITAM in Mexico. His research interests are focused on nonlinear and adaptive control, stability analysis and the state estimation problem, with application to mechanical systems, aerial vehicles, mobile robots and multi-agent systems. He currently serves as an Editor of the INTERNATIONAL JOURNAL OF ADAPTIVE



(2022). He is the Corresponding Co-Chair of IEEE Technical Committee on Collaborative Automation for Flexible Manufacturing (CAF), and a Fellow of British Computer Society. His research interest lies in human robot interaction and intelligent system design.

Chenguang Yang (M'10-SM'16) received the Ph.D. degree in control engineering from the National University of Singapore, Singapore, in 2010, and postdoctoral training in human robotics from the Imperial College London, London, U.K. He was awarded UK EPSRC UKRI Innovation Fellowship and individual EU Marie Curie International Incoming Fellowship. As the lead author, he won the IEEE Transactions on Robotics Best Paper Award (2012) and IEEE Transactions on Neural Networks and Learning Systems Outstanding Paper Award



IEEE TRANSACTIONS ON ROBOTICS.

David Navarro-Alarcon (Senior Member, IEEE) received the Ph.D. degree in mechanical and automation engineering from The Chinese University of Hong Kong, in 2014. Since 2017, he has been with The Hong Kong Polytechnic University, where he is currently an Associate Professor with the Department of Mechanical Engineering, and the Principal Investigator of the Robotics and Machine Intelligence Laboratory. His current research interests include perceptual robotics and control systems. He currently serves as an Associate Editor of the